Pergamon

Geochimica et Cosmochimica Acta, Vol. 68, No. 22, pp. 4679-4686, 2004

0016-7037/04 $30.00 + .00

doi:10.1016/j.gca.2004.04.018

Nanoscale occurrence of Pb in an Archean zircon

SATOSHI UTSUNOMIYA,[1] CHRIS S. PALENIK,[1] JOHN W. VALLEY,[2] AARON J. CAVOSIE,[2] SIMON A. WILDE,[3] and RODNEY C. EWING[1,*]

[1]Geological Sciences, University of Michigan, 425 East University Avenue, Ann Arbor, MI 48109-1063, USA
[2]Department of Geology and Geophysics, University of Wisconsin, 1215 West Dayton Street, Madison, WI 53706, USA
[3]Department of Applied Geology, Curtin Institute of Technology, GPO Box U1987, Perth, Australia

(*Received November* 11, 2003; *accepted in revised form April* 26, 2004)

Abstract—We report, for the first time, a direct, atomic-scale characterization of Pb in zircon (4.4–3.1 Ga) from the early Archean Yilgarn craton in Australia using high-resolution HAADF-STEM. Two forms of Pb have been identified: Pb concentrated at ~3 atom% as a nanoscale patch in zircon structure, and Pb concentrated within the amorphous domain created by fission fragment damage. The first result suggests that the Pb atoms directly substitute for Zr^{4+} in the zircon structure, and the latter observation demonstrates that Pb diffusion can occur through amorphous regions created by radiation damage, although volume diffusion is typically considered to be the dominant mechanism for Pb diffusion. Beyond the first percolation point, i.e., when the amorphous domains overlap and form a fully interconnected network of amorphous domains, there is a new pathway for the diffusion of Pb that is faster than volume diffusion through crystalline zircon. *Copyright © 2004 Elsevier Ltd*

1. INTRODUCTION

Zircon ($ZrSiO_4$) is one of the most thoroughly studied of natural phases because of its predominant use in geochronology (Krogh, 1982; Bowring and Housh, 1995; Vervoort et al., 1996; Bowring et al., 1989; Amelin et al., 1999) and oxygen isotope studies (Valley, 2003). Because zircon is physically and chemically durable (Ewing, 1999), it has also been proposed as a waste form for the immobilization of plutonium from dismantled nuclear weapons (Ewing et al., 1995; Ewing, 1999). In each of these applications, loss of trace elements, e.g., U, Pb and Pu, is of critical interest, and elemental loss may be much enhanced by radiation damage caused by the α-decay of constituent actinides, ^{232}Th, ^{235}U, ^{238}U, and radionuclides in their decay series (Ewing, 2003). The fate of Pb is critical in U-Th-Pb isotopic dating, because Pb-loss due to radiation-enhanced alteration of zircon is a common cause of discordant dates (Pidgeon et al., 1966; Craig, 1968).

The diffusion of Pb, coupled with the diffusion of U and Th, has been extensively studied, and the Pb-diffusion rate is generally considered to be faster than that of the tetravalent actinides U, Th and Pu (Bogomolov, 1991; Cherniak et al., 1997; Lee et al., 1997; Watson et al., 1997; Cherniak and Watson, 2000). The diffusivities of tetravalent cations, U, Th and Hf, in synthetic zircon were found to increase with decreasing ionic radius (Cherniak et al., 1997). Diffusion coefficients of U, Th and Pb have been systematically measured, the Pb diffusion coefficient is ~4 orders of magnitude greater than that of U and Th at 1100°C (Lee et al., 1997), and the difference may be as high as ~6 orders of magnitude (Cherniak and Watson, 2000). Recently, estimates of inward and outward diffusion rates of Pb in zircon have been reexamined at 1200–1300°C, and the measured rates are 1–2 orders of magnitude slower than the previously determined values (Cherniak and Watson, 2000); nonetheless, Pb diffusion is still considerably faster than that of tetravalent U and Th.

In addition to volume diffusion, amorphous domains created by radiation damage provide an additional pathway for Pb diffusion. The accumulation of radiation damage in zircon results from the α-decay series for ^{238}U, ^{235}U, and ^{232}Th to ^{206}Pb (eight α-decay events), ^{207}Pb (seven α-decay events), and ^{208}Pb (six α-decay events), respectively. The α-decay event causes radiation damage to the atomic-scale periodicity by two separate, simultaneous process; (i) an alpha particle (helium nucleus) with an energy of ~4.5 to 5.8 MeV dissipates most of its energy by electronic excitations along a trajectory of 10–30 μm, and (ii) an alpha recoil atom with an energy of 70 to 100 keV transfers most of its energy through elastic collisions creating a displacement cascade of approximately 1000 atoms. (Ewing et al., 1987, 2000, 2003). With accumulating radiation damage, the overlap of these amorphous domains creates interconnected pathways that may provide fast paths for diffusion. The formation of these pathways has been described and modeled using percolation theory, which defines two percolation points (Salje et al., 1999; Ríos et al. 2000; Trachenko et al., 2003). At the first percolation point, the concentration of amorphous domains is large enough to form an interconnected pathway of overlapping amorphous domains. At this point there should be an increase in the diffusivity. At the second percolation point, the formerly interconnected crystalline matrix is reduced to a series of disconnected crystalline "islands" in an amorphous matrix.

Based on crystal chemistry and experimental data, U and Th are known to substitute into the ZrO_7 coordination polyhedron of zircon as tetravalent cations (Speer, 1982). However, there is no consensus concerning the atomic location of Pb produced by the α-decay of U and Th. Pb may occupy the Zr-site or be present in the amorphous domains created by α-decay events. Indeed, a high concentration of Pb implanted into zircon was reported to form nanocrystals (Lian et al., 2003). Although a previous study (Cherniak and Watson, 2000) has pointed out that the valence of Pb in zircon must affect the Pb diffusion

* Author to whom correspondence should be addressed, at Department of Geological Sciences, 425 East University Avenue, Ann Arbor, MI 48109-1063 (rodewing@umich.edu).

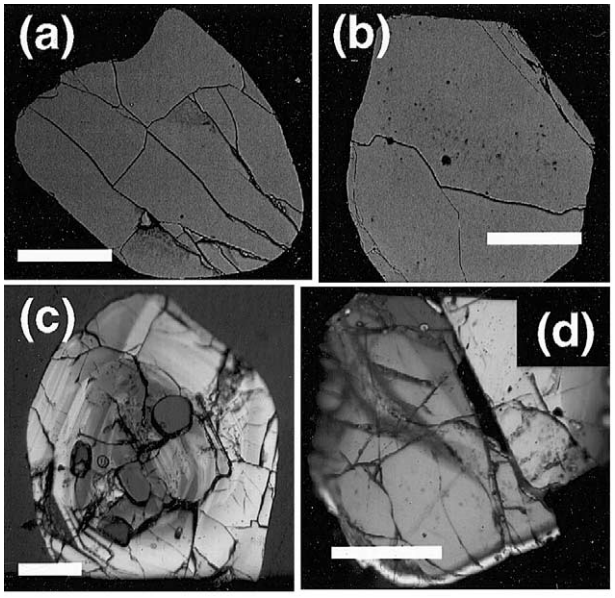

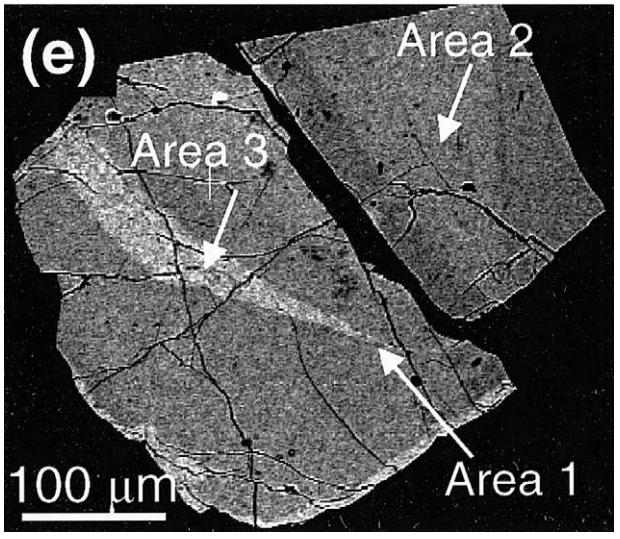

Fig. 1. Texture of the zircon from the Jack Hills, Western Australia. BSE images (a and b) and polarized optical micrographs (c and d). Scale bars are 100 μm. (e) The BSE image of the grain shown in (d).

rate, the form of Pb within zircon has never been determined. Pb atoms typically occur at low concentrations (ppm levels) in the zircon structure, and as a result the spatial resolution of the techniques used to study zircon (X-ray diffraction, ion microprobe, and Raman spectroscopy) are not sufficient to directly observe Pb atoms or even regions enriched in Pb.

In this study, we have examined zircon crystals from the Jack Hills metasedimentary belt (Amelin et al., 1999; Peck et al., 2001; Wilde et al., 2001; Valley et al., 2002; Valley, 2003) using high-resolution transmission electron microscopy (HRTEM) and related nanobeam techniques to determine the location and distribution of Pb within zircon. Ten detrital zircon grains from a sample of Jack Hills conglomerate (sample 01-JH-54) have been studied. Cavosie et al. (2004) analyzed the sample group 01-JH-54 using secondary ion mass spectrometry and reported that the age of the group is within the range of 4.4 to 3.1 Ga.

2. EXPERIMENTAL METHODS

Back-scattered electron (BSE) imaging was completed using a HITACHI S-3200N SEM. The chemical composition was determined by electron microprobe analysis (EMPA) using a CAMECA SX50. Accelerating voltage was 20 keV and the beam current was 80 nA. The Cameca PAP correction was used to reduce the data. Standards used were zircon for Hf (Mα), Zr (Lα) and Si (Kα), thorite for Th (Mα) and UO_2 for U (Mα) and PbS for Pb (Mα). Detection limits for U, Th and Pb were 300, 250 and 300 ppm, respectively. The low analytical totals obtained during EMPA analysis (Table 1) are due largely to the limited thickness and tilt of the sample relative to the standards. Before analysis, the zircon crystals were mounted on TEM grids and polished to a wedge with a thickness of <10 μm as described below.

Zircon grains (<500 μm in diameter) were individually molded in M-bond and cured. The mold was trimmed into a 2×2 mm square. The crystal and epoxy were mechanically polished to a thickness of less than 10 μm and secured to a molybdenum grid. The specimen was subsequently milled by a 4.0 keV Ar ion beam using a GATAN precision polishing system. The TEM specimen holder was cleaned with plasma (Fischione Model C1020) to minimize hydrocarbon contamination. HRTEM and nanoscale elemental mapping were completed by high-angle annular dark-field scanning transmission electron microscopy (HAADF-STEM) using a JEOL JEM2010F coupled with Emispec ES Vision version 4.0 for STEM-EDX (energy dispersive X-ray analysis) mapping. To minimize the effect of sample drift, the drift-correction mode was used during the acquisition of EDX maps. STEM specifications: Cs = 1.0 mm, probe size is 1.0 nm for analysis and 0.2 nm for high resolution imaging, the collection angle of HAADF detector is 50–110 mrad, the objective aperture size used is 30 μm for analysis and 20 μm for high resolution imaging, the defocus condition is approximately -55 nm. Image processing, including the fast Fourier transformation (FFT), was completed using Gatan Digital Micrograph 3.4.

Raman spectra were collected at the micro-Raman laboratory of the University of Michigan. The excitation source is provided by a 6 W Ar-ion continuous-wave laser from which the 514.5 nm line is used. An Olympus BH-2 microscope equipped with a Mitatoyo 50$\times$ objective is used to focus the laser to a spot of 2 μm on the single crystal. The scattered radiation is analyzed with a Spex 1250 spectrometer equipped with a 600 g/mm holographic grating and collected by a cooled CCD detector. Coupled with a 150 mm confocal slit, the spectral resolution

Table 1. Chemical composition (wt%) of the zircon (Fig. 1e) by EMPA

	ZrO_2	SiO_2	HfO_2	PbO	ThO_2	UO_2	Total
Brighter contrast (n = 7)	63.8 (2.6)	30.8 (0.18)	1.40 (0.18)	0.03 (0.02)	0.14 (0.02)	0.09 (0.02)	96.2
Darker contrast (n = 7)	64.1 (2.7)	31.1 (0.18)	1.40 (0.17)	BDL	BDL	BDL	96.6

Results are the averaged compositions taken from multiple microprobe analyses in the bright (n = 7) and dark (n = 6) contrast areas (high and low actinide content areas) of the BSE image shown in Figure 1e. The numbers in parentheses represents the analytical standard deviations. The low analytical totals can be largely attributed to the thickness of the sample ($<$ 10 μm), which was required for TEM analysis. BDL = Below Detection Limits.

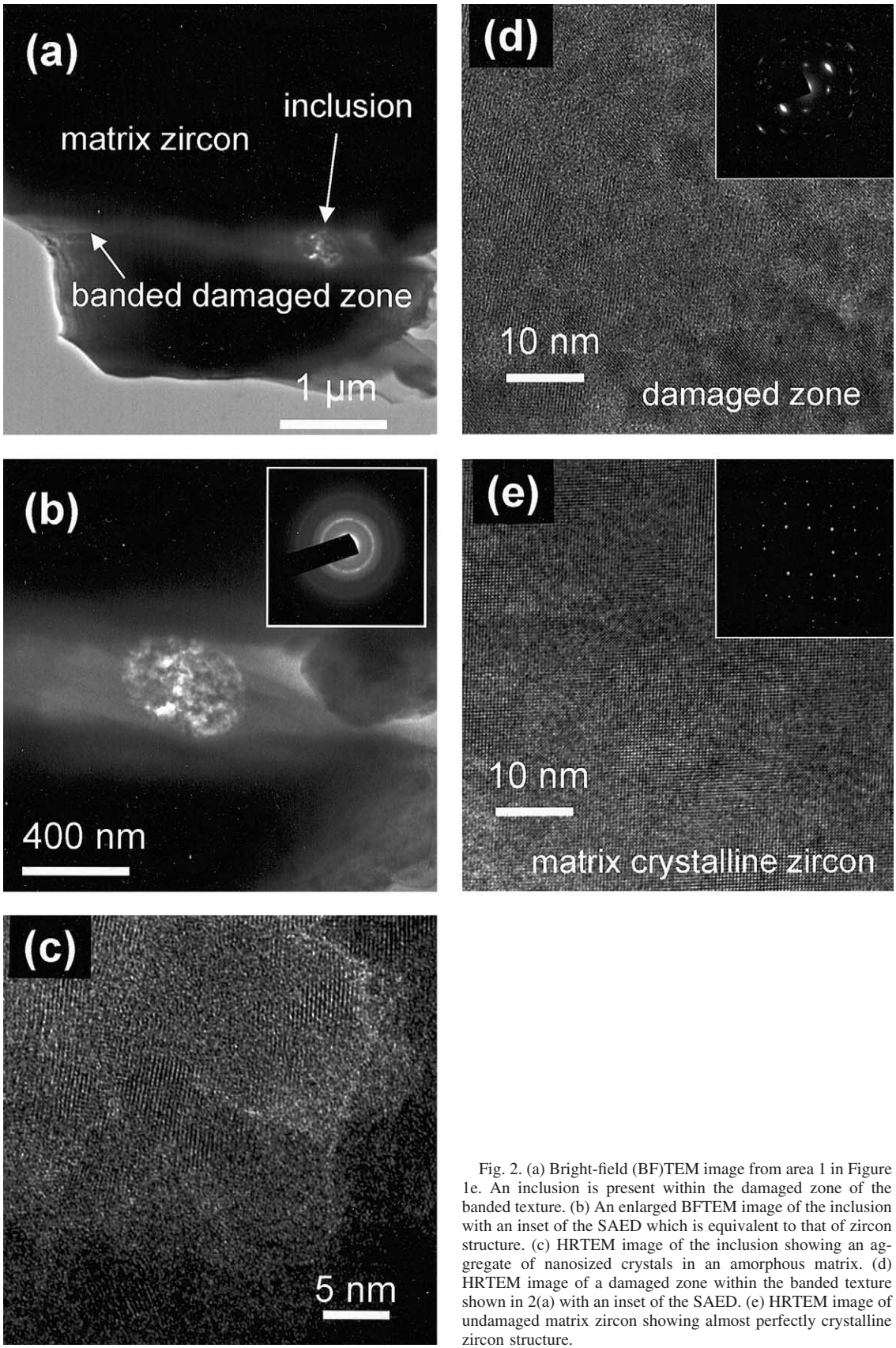

Fig. 2. (a) Bright-field (BF)TEM image from area 1 in Figure 1e. An inclusion is present within the damaged zone of the banded texture. (b) An enlarged BFTEM image of the inclusion with an inset of the SAED which is equivalent to that of zircon structure. (c) HRTEM image of the inclusion showing an aggregate of nanosized crystals in an amorphous matrix. (d) HRTEM image of a damaged zone within the banded texture shown in 2(a) with an inset of the SAED. (e) HRTEM image of undamaged matrix zircon showing almost perfectly crystalline zircon structure.

was 5 cm^{-1}. Raman shifts ranging from 150 to 1200 cm^{-1} were measured with laser power of 1 W. Three accumulations of 60 s were integrated. Full width at half maximum measurements of the $B1_g(\nu_3)$ mode at 1008 cm^{-1} measurements were made by fitting two Gaussian-Lorentzian peaks using PeakFit V4 as described in Palenik et al. (2003). The FWHM measurements were corrected for spectrometer resolution using the simplified apparatus function described by Imer (1985). Conservative errors of 10% were assigned to the measured FWHM values based on the variations in the different means by which the Raman spectrum can be fit.

3. RESULTS AND DISCUSSION

BSE images of most of the zircon grains (Figs. 1a,b) showed no change in Z-contrast within the grain in BSE, while a few grains showed zoning and quartz inclusions (Fig. 1c) or large changes in retardation (Fig. 1d) under crossed-polars optical microscopy. A BSE image of the grain in Figure 1d revealed relatively high Z-contrast domains within the grain. The elemental composition (Table 1) indicates that the bright-contrast zone within the zircon contains relatively high concentrations of U, Th, and Pb (average concentrations: 0.09, 0.14, and 0.03 wt%, respectively) as compared with the darker regions where the average concentrations were below the detection limits of the EMPA. Based on the average U and Th concentrations of this region (Fig. 1e), the dose can be calculated to be 17×10^{15} α-decay events/mg, equivalent to 0.8 dpa (displacement per atom). An unannealed zircon typically becomes fully amorphous at a dose of ~0.3 dpa (Meldrum et al., 1998), which suggests that this sample has undergone significant annealing. Micro-Raman spectroscopy of this sample confirms that annealing has occurred. See the Appendix for a more complete discussion of annealing in this sample.

Some areas in the actinide- and Pb-rich zone (areas 1 to 3 in Fig. 1e) were subsequently observed at the nanoscale. In area 1, shown in more detail in a TEM image (Fig. 2a), a banded texture, a few hundred nanometers in width, occurs with a 400 nm inclusion that can be seen adjacent to the undamaged matrix zircon. Semiquantitative analysis indicates that the concentrations of U and Th in the damaged zone were 1.9 and 3.9 wt%, respectively, and in the inclusion the U and Th were 5.6 and 11 wt%, respectively, in the inclusion. Thus nanoscale inclusions can partially account for the higher actinide contents measured by EMPA in area 1, as well as the elevated Th concentration (relative to U). Pb was not detected in the either region by EDX. Selected area electron diffraction (SAED) of the inclusion revealed a ring pattern (Fig. 2b), which is consistent with the structure of zircon. A HRTEM image of the inclusion showed an aggregate of nanocrystals of a few nanometers in diameter and an amorphous matrix (Fig. 2c). A HRTEM image of the damaged zone shows amorphous domains with slightly rotated crystalline fragments revealed by SAED (Fig. 2d), while the area labeled matrix zircon with undetectable amounts of U and Th shows a perfectly crystalline structure (Fig. 2e).

Area 2 (Fig. 1e), shows a narrow, banded texture with detectable amounts of U and Th by EDX (Fig. 3a) similar to that of area 1. The HRTEM image of the banded region reveals a highly damaged area consisting of isolated crystallites in an amorphous matrix of overlapping α-recoil cascades (Fig. 3b). The banded damaged regions are ~100 nm wide and >1 μm long. No Pb was detected in these regions. This texture of narrow, damaged regions is similar to the nanoscale zoning

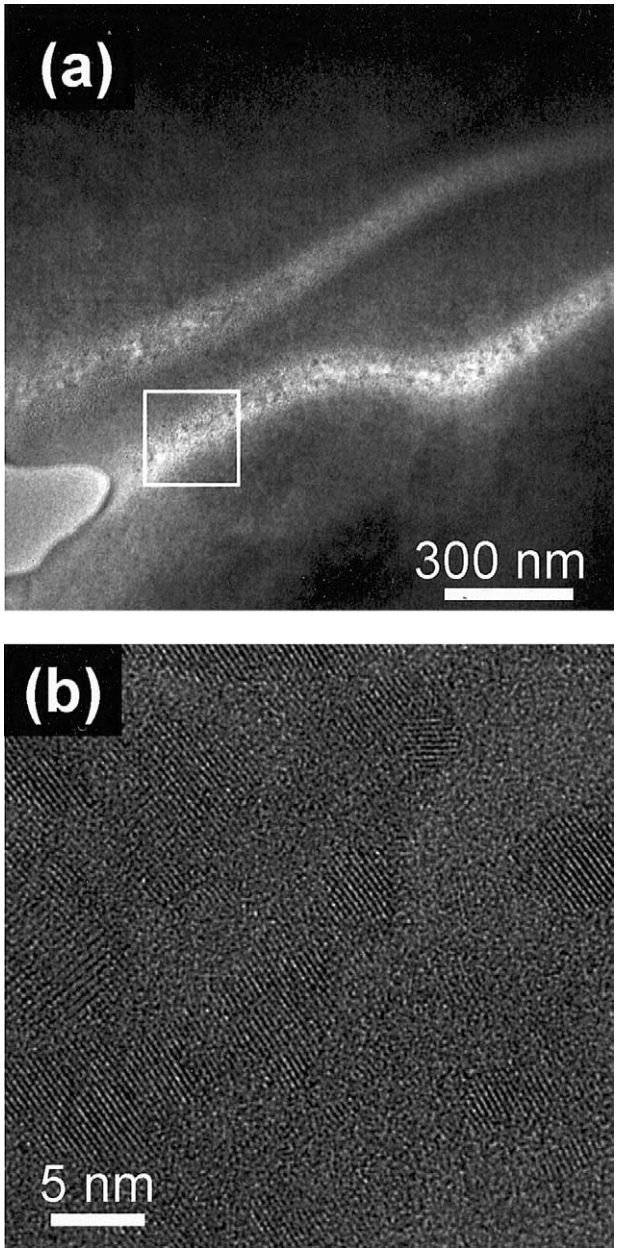

Fig. 3. (a) BFTEM image of area 2 in Figure 1e showing long damaged zones (>1 μm) with a width of ~150 nm. (b) HRTEM image of the boxed area in (a) showing a damaged structure with a large amorphous fraction.

observed in a previous study of radiation damage in zircon, suggesting that zoning occurs on a much finer scale than is evident optically (Palenik et al., 2003).

Another possibility for the enrichment of the actinides and Pb in the regions of bright contrast is recrystallization from hydrothermal fluids. Indeed, Watson et al. (1997) successfully synthesized zircon containing >3 atomic% of Pb by an epitaxial growth over pure zircon substrates.

The high U, Th and Pb region was further investigated in an attempt to locate the Pb using HAADF-STEM (Utsunomiya and Ewing, 2003). HAADF-STEM imaging provides a Z-contrast image in which Pb-rich regions appear brighter against

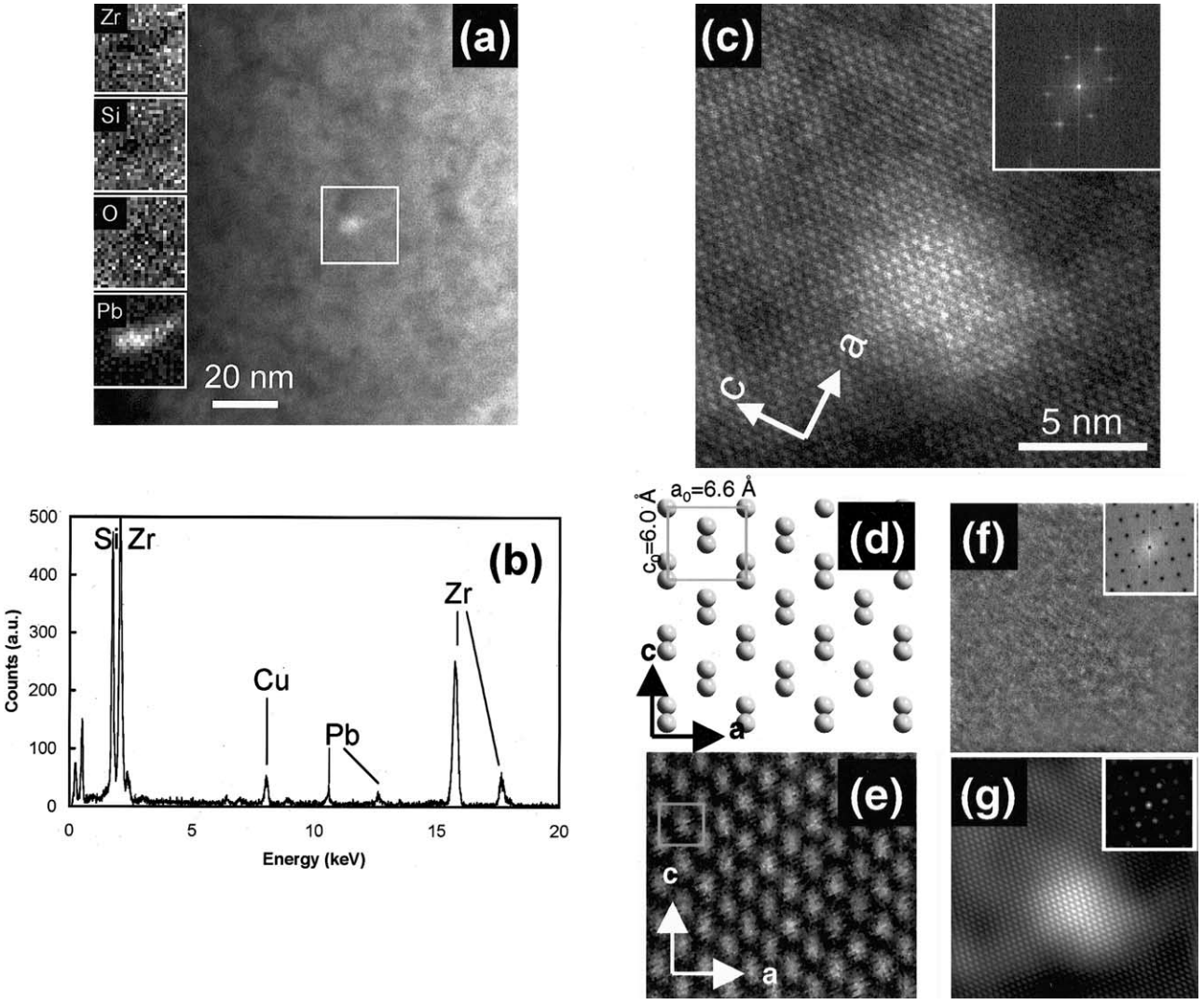

Fig. 4. Patchy concentrations of Pb in zircon. (a) HAADF-STEM image with elemental maps of the boxed region. (b) The EDX spectrum of the bright region in (a) analyzed by nanoprobe (1 nm in the diameter). (c) High resolution HAADF-STEM image from the view along [010] with the inset of the FFT (Fast Fourier Transformed) image. (d) The projected position of Zr atoms in zircon structure along [010], based on the configuration of Zr atoms in zircon (Yada et al., 1987). The radius of the ball is scaled to the ionic radius of Zr^{4+}. The rectangular box represents the unit cell. (e) A typical image of pure zircon using high resolution HAADF-STEM. The relatively heavier element, Zr, shows the brightest contrast compared to Si and O. (f) The inverse FFT image from the opaquely masked diffraction pattern (inset). (g) The inverse FFT image from the masked diffraction (inset).

the lower average atomic mass of the zircon matrix. The HAADF-STEM image of area 3 revealed some relatively high contrast patches (~5 nm in diameter) (Fig. 4a), and nanoscale elemental maps showed higher concentrations of Pb. The Zr-content was significantly depleted in the Pb-rich region, while the Si-distribution in the same region does not show any detectable depletion (Fig. 4a). Semiquantitative analysis indicated that the concentration of Pb in the white spots was ~5.6 wt% (Fig. 4b). The actual Pb concentration may be higher, because of the larger interaction volume of the electron beam with the surrounding zircon matrix.

High-resolution (HR-) HAADF-STEM images of a Pb-rich region show a continuous zircon structure across the Pb-rich region (Fig. 4c). Because the HR-HAADF-STEM image is formed by an incoherent imaging process (Pennycook and Jesson, 1990), the Pb atoms simply appear as brighter spots. In the case of pure zircon, $ZrSiO_4$, Zr atoms appear as relatively bright spots as compared with Si and O (Figs. 4d,e). The FFT image of Figure 4c was masked to extract structural information (Figs. 4f,g). These filtered images suggest that; (i) Pb atoms were incorporated directly into the zircon structure, and (ii) there is no other phase that contains Pb (Figs. 4f,g). The distribution of Pb in this area (Fig. 4a) and the structural information provided by high resolution HAADF-STEM (Fig. 4c) suggests that Pb directly substitutes for Zr in the zircon structure. In terms of the circumstances of Pb incorporation at Zr site, the common valence, Pb^{2+}, has ionic radius of 1.29 Å which is considerably larger than that of Zr^{4+}, 0.84 Å (Shan-

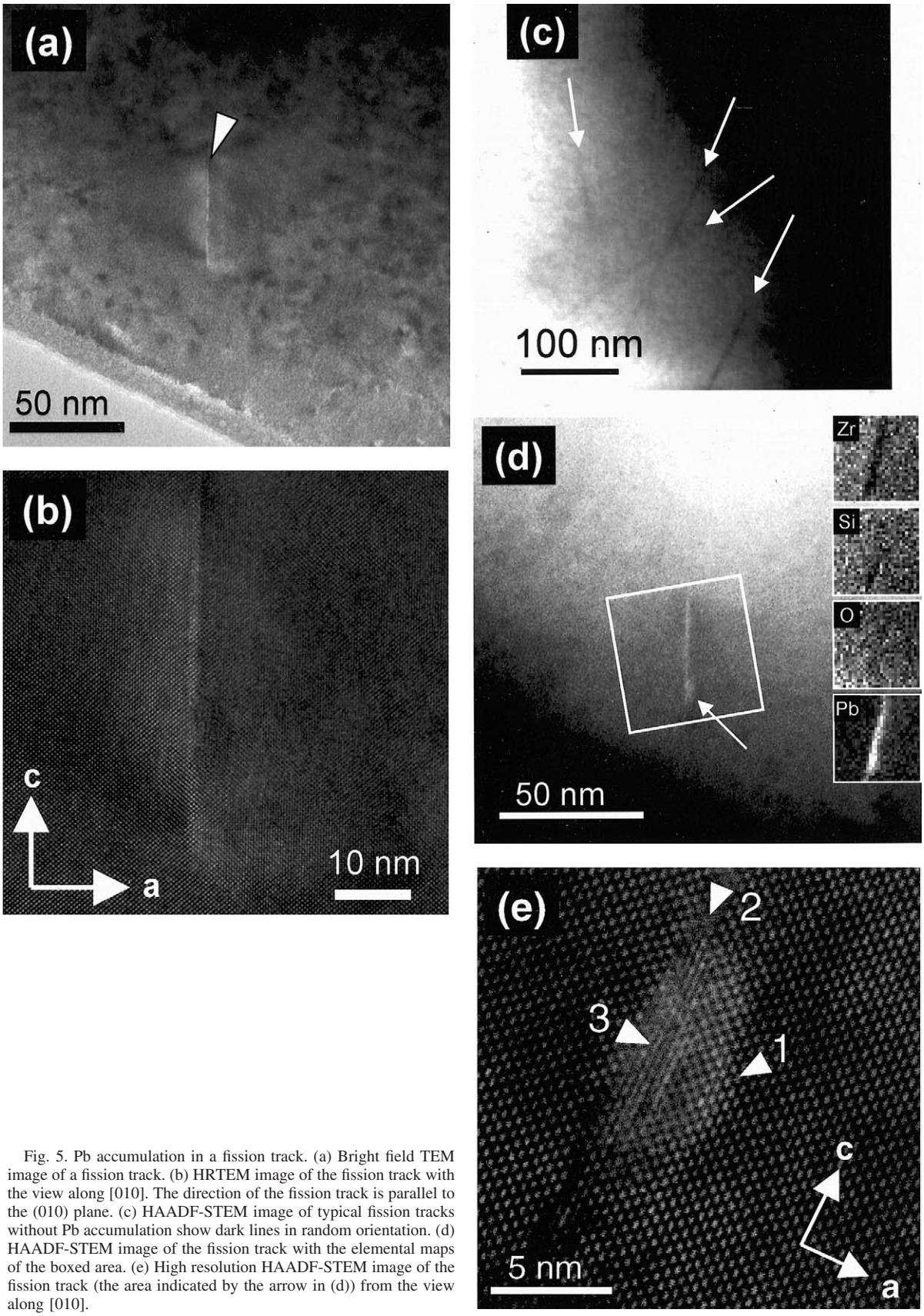

Fig. 5. Pb accumulation in a fission track. (a) Bright field TEM image of a fission track. (b) HRTEM image of the fission track with the view along [010]. The direction of the fission track is parallel to the (010) plane. (c) HAADF-STEM image of typical fission tracks without Pb accumulation show dark lines in random orientation. (d) HAADF-STEM image of the fission track with the elemental maps of the boxed area. (e) High resolution HAADF-STEM image of the fission track (the area indicated by the arrow in (d)) from the view along [010].

non, 1976). A less common valence, Pb^{4+}, has an ionic radius (Pb^{4+} = 0.94 Å), compatible with possible substitution of Zr^{4+}. Despite the size preference for Pb^{4+}, the Pb-O system is dominated by PbO under typical geological conditions, with a small stability field for native Pb. The stability field for PbO_2 exists only under far more oxidizing conditions (Watson et al., 1997). However, it is possible that the compatibility of the size and charge can result in stabilization of the tetravalent oxidation state in the zircon structure. Because the concentration of Pb at this patch is only ~3 atomic%, it is difficult to draw any conclusions about the valence of Pb using only the structural information obtained from the HRSTEM image.

In addition to the patchy occurrence of Pb, the Pb-rich area also revealed numerous fission tracks (<5 nm width) created by high-energy (~100 MeV), heavy particles from spontaneous fission events (Figs. 5a,b). Although spontaneous fission of ^{238}U is infrequent (decay constant = 10^{-16}/yr (Yada et al., 1987)), the old age and actinide content of these zircons suggest that fission tracks are to be expected. Although a fission track is typically up to 10 μm in length (Yada et al., 1981), the length of fission tracks observed here are ~50 nm. The observable length is limited mainly by the thickness of the imaged specimen, which depends on the thickness through which a 200 keV electron can penetrate and the random orientation of fission tracks in three dimensions. The majority of the fission tracks were visible as streaks of dark contrast in the HAADF-STEM images (Fig. 5c); however, one fission track showed bright contrast (Fig. 5d) throughout the length of the entire track. The elemental maps indicated that this fission track had a higher concentration of Pb than the matrix. The orientation of this fission track is parallel to the (011) plane (Fig. 5b), which is consistent with channeling of fission fragment in the structure (Yada et al., 1987). The high resolution HAADF-STEM image of the end of this fission track (Fig. 5e) shows: (I) The edge of the zircon lattice, indicated by an arrow 1, has a higher contrast than the bulk zircon matrix, suggesting the incorporation of Pb atoms in the zircon lattice adjacent to the fission track. This is also supported by the Pb elemental map in Figure 5d. (II) There is no continuous lattice within the track (arrow 2). The interface between the zircon matrix and the fission track (arrow 3), shows a disordered array of bright contrast, suggesting that the accumulated Pb is not in a crystalline phase or, if crystalline, without any preferred orientation relative to the surrounding zircon structure. In addition, the oxygen distribution in this area does not show any evidence of O-depletion in the fission track, which indicates that Pb is not present as elemental Pb.

The occurrence of Pb in the fission track is obviously not original, since spontaneous fission occurred after zircon formation. Thus, Pb probably accumulated in the track by diffusion, which, in the case of the images shown in Figures 5d and e, appears to be at the end of the fission track. A similar texture of U or Th accumulation in the fission track was not observed. In general, fission tracks are amorphous regions (Yada et al., 1981), as anticipated by irradiation experiments using highly-energetic heavy ions (Ewing et al., 2003). The Pb that has accumulated in the fission track observed here suggests that Pb can diffuse through an amorphous domain, such as fission tracks, as well as metamict domains resulting from the accumulation of α-decay event damage (e.g., the banded amorphous regions in Figs. 2 and 3). In fact, previous experiments (Cherniak et al., 1991; Cherniak, 1993) on the Pb diffusion rate in zircon have predicted that Pb diffusion through highly damaged paths would show a higher diffusion rate. The above observations are consistent with the percolation theory model of radiation damage accumulation in zircon, whereby, radiation damage accumulation results first in the formation of isolated amorphous domains that then overlap as the damage accumulates, eventually creating a network of interconnected amorphous domains that could serve as a fast diffusion pathway (Salje et al., 1999; Ríos et al., 2000; Trachenko et al., 2003). The first percolation point is defined as the dose at which the damaged amorphous domains become fully interconnected. These results show the potential significance of Pb diffusion through amorphous domains that result from radiation-damage.

Acknowledgments—S.U. thanks J. F. Mansfield and C. J. Wauchope for their technical support in the Electron Microbeam Analysis Laboratory at the University of Michigan and M. Kawasaki and S. Johnson of JEOL, USA, for important advice on the use of the STEM. We very much appreciate the constructive review comments by Professor Bruce Watson, Dr. David Cole, and two anonymous reviewers. We thank Professor Lars Stixrude for access to the Raman microprobe (supported by NSF EAR99-73050 to L. Stixrude). This work was supported by the Division of Materials Science of the Office of Basic Energy Science of the U.S. Department of Energy (DE-FG02-97ER45656).

Associate editor: D. Cole

REFERENCES

Amelin Y., Lee D. C., Halliday A. N., and Pidgeon R. T. (1999) Nature of the Earth's earliest crust from hafnium isotopes in single detrital zircons. *Nature* **399,** 252–255.

Bogomolov Ye. S. (1991) Migration of lead in non-metamict zircon. *Earth Planet. Sci. Lett.* **107,** 625–633.

Bowring S. A. and Housh T. (1995) The Earth's early evolution. *Science* **269,** 1535–1540.

Bowring S. A., King J. E., Housh T. B., Isachsen C. E., and Podosek F. A. (1989) Neodymium and lead isotope evidence for enriched early Archaean crust in North America. *Nature* **340,** 222–225.

Cavosie A. J., Wilde S. A., Liu D., Valley J. W., and Weiblen P. W. (2004) Internal zoning and U-Th-Pb chemistry of Jack Hills detrital zircons: A mineral record of Early Archean (4404-1576 Ma) magmatism. Precambrian Research. (in press).

Cherniak D. J. (1993) Lead diffusion in titanite and preliminary results on the effects of radiation damage on Pb transport. *Chem. Geol.* **110,** 177–194.

Cherniak D. J., Lanford W. A., and Ryerson F. J. (1991) Lead diffusion in apatite and zircon using ion implantation and Rutherford Backscattering techniques. *Geochim. Cosmochim. Acta* **55,** 1663–1673.

Cherniak D. J., Hanchar J. M., and Watson E. B. (1997) Diffusion of tetravalent cations in zircon. *Contrib. Mineral. Petrol.* **127,** 383–390.

Cherniak D. J. and Watson E. B. (2000) Pb diffusion in zircon. *Chem. Geol.* **172,** 5–24.

Craig H. (1968) Zircon lead loss—A kinetic model. *Science* **159,** 447.

Ewing R. C., Lutz W., and Weber W. J. (1995) Zircon: A host-phase for the disposal of weapons plutonium. *J. Mater. Res.* **10,** 253–246.

Ewing R. C. (1999) Nuclear waste forms for actinides. *Proc. Nat. Acad. Sci. USA* **96,** 3432–3439.

Ewing R. C., Chakoumakos B. C., Lumpkin G. R., and Murakami T. (1987) The metamict state. *Mater. Res. Soc. Bull.* **12,** 58–66.

Ewing R. C., Meldrum A., Wang L. M. and Wang S. X. (2000) Radiation-induced amorphization. In *Transformation Processes in Minerals* (eds. S. A. T. Redfern and M. A. Carpenter), pp. 319–361. Rev. Mineral. Geochem. 39. Mineralogical Society of America.

Ewing R. C., Meldrum A., Wang L. M., Weber W. J., and Corrales L. R. (2003) Radiation damage in zircon. In *Zircon* (eds. J. M.

Hanchar and P. W. O. Hoskin), pp. 387–425. Rev. Mineral. Geochem. 53. Mineralogical Society of America.
Imer G. (1985) Zum Einfluss der Apparatefunktion auf die Bestimmung von Streuquerschnitten und Lebensdauern aus optishchen Phononenspectren. *Exp. Tech. Phys.* **33,** 501–506.
Krogh T. E. (1982) Improved accuracy of U-Pb zircon ages by the creation of more concordant systems using an air abrasion technique. *Geochim. Cosmochim. Acta* **46,** 637–649.
Lee J. K. W., Williams I. S., and Ellis D. J. (1997) Pb, U and Th diffusion in natural zircon. *Nature* **390,** 159–162.
Lian J., Ríos S., Boatner L. A., Wang L. M., and Ewing R. C. (2003) Microstructural evolution and nanocrystal formation in Pb^{+}-implanted $ZrSiO_4$ single crystals. *J. Appl. Phys.* **94,** 5695–5703.
Meldrum A., Zinkle S. J., Boatner L. A., and Ewing R. C. (1998) A transient liquid-like phase in the displacement cascades of zircon, hafnon and thorite. *Nature* **395,** 56–58.
Nasdala L., Wenzel M., Vavra G., Irmer G., Wenzel T., and Kober B. (2001) Metamictisation of natural zircon: Accumulation versus thermal annealing of radioactivity-induced damage. *Contrib. Mineral. Petrol.* **141,** 125–144.
Nasdala L., Reiners P. W., Garver J. I., Kennedy A. K., Stern R. A., Balan E., and Wirth R. (2004) Incomplete retention of radiation damage in zircon from Sri Lanka. *Am. Mineral.* **89,** 219–231.
Palenik C. S., Nasdala L., and Ewing R. C. (2003) Radiation damage in zircon. *Am. Mineral.* **88,** 770–781.
Peck W. H., Valley J. W., Wilde S. A., and Graham C. M. (2001) Oxygen isotope ratios and rare earth elements in 3.3 to 4.4 Ga zircons: Ion microprobe evidence for high $\delta^{18}O$ continental crust and oceans in the Early Archean. *Geochim. Cosmochim. Acta* **65,** 4215–4229.
Pennycook S. J. and Jesson D. E. (1990) High-resolution incoherent imaging of crystals. *Phys. Rev. Lett.* **64,** 938–941.
Pidgeon R. T., O'Neil J. R., and Silver L. T. (1966) Uranium and lead isotopic stability in a metamict zircon under experimental hydrothermal conditions. *Science* **154,** 1538–1540.
Ríos S., Salje E. K. H., Zhang M., and Ewing R. C. (2000) Amorphization in zircon: Evidence for direct impact damage. *J. Phys. Condensed Matt.* **12,** 2401–2412.
Salje E. K. H., Chrosch J., and Ewing R. C. (1999) Is "metamictization" of zircon a phase transition? *Am. Mineral.* **84,** 1107–1116.
Shannon R. D. (1976) Revised effective ionic radii and systematic studies of interatomic distances in halides and chalcogenides. *Acta Crystallogr. A* **32,** 751–767.
Speer J. A. (1982) Zircon. In *Orthosilicates* (ed. P. H. Ribbe), pp. 67–112. Reviews in Mineralogy **5,** Mineralogical Society of America.
Trachenko K., Dove M. T., and Salje E. K. H. (2003) Large swelling and percolation in irradiated zircon. *J. Phys. Condensed Matt.* **15,** L1–L7.
Utsunomiya S. and Ewing R. C. (2003) Application of high-angle annular dark field scanning transmission electron microscopy—energy dispersive X-ray spectrometry, and energy-filtered transmission electron microscopy to the characterization of nanoparticles in the environment. *Environ. Sci. Technol.* **37,** 786–791.
Valley J. W. (2003) Oxygen isotopes in zircon. In *Zircon* (eds. J. M. Hanchar and P. W. O. Hoskin), pp. 343–385. Reviews in Mineralogy **53,** Mineralogical Society of America.
Valley J. W., Peck W. H. King E. M., and Wilde S. A. (2002) Cool early Earth. *Geology* **30,** 351–354.
Vervoort J. D., Patchett P. J., Gehrels G. E., and Nutman A. P. (1996) Constraints on early Earth differentiation from hafnium and neodymium isotopes. *Nature* **379,** 624–627.
Watson E. B., Cherniak D. J., Hanchar J. M., Harrison T. M., and Wark D. A. (1997) The incorporation of Pb into zircon. *Chem. Geol.* **141,** 19–31.
Wilde S. A., Valley J. W. Peck W. H., and Graham C. M. (2001) Evidence from detrital zircons for the existence of continental crust and oceans on the Earth 4.4 Gyr ago. *Nature* **409,** 175–178.
Yada K., Tanji T., and Sunagawa I. (1981) Application of lattice imagery to radiation damage investigation in natural zircon. *Phys. Chem. Miner.* **7,** 47–52.
Yada K., Tanji T., and Sunagawa I. (1987) Radiation induced lattice defects in natural zircon ($ZrSiO_4$) observed at atomic resolution. *Phys Chem. Miner.* **14,** 197–204.

APPENDIX

Based on the U and Th concentration analyzed by EMPA, the dose accumulated in the brighter contrast area (Fig. 1e) can be calculated to be 17×10^{15} α-decay events/mg, equivalent to 0.8 dpa. Refer toPalenik et al. (2003) for the details of the dose calculations. Although the accumulated dose calculated using EMPA data was 0.8 dpa and zircon should become fully amorphous at ~0.3 dpa at room temperature (Meldrum et al., 1998), nanoscale observation by HRTEM did not reveal any fully amorphous regions (Figs. 2 and 3).

Micro-Raman spectroscopy carried out on this zircon sample confirms TEM evidence that the Jack Hill zircons have not completely retained their radiation damage. A plot of radiation damage versus peak width (full width at half maximum—FWHM) for the $B1_g(\nu_3)$ mode at 1008 cm^{-1} is shown in Fig. A1. The dose, plotted along the abscissa is a measure of the number of α-decay events experienced by a sample. FWHM data is proportional to the actual amount of damage present in the zircon structure and increases as the amount of damage increases and the sample becomes more amorphous. Annealing or recrystallization of radiation damage results in a decrease in FWHM. The line plotted in Fig. A1 corresponds to the dose-damage profile for a zircon that has completely retained its radiation damage (i.e., has not experienced annealing) (Palenik et al., 2003).

The FWHM data from two of the Archean zircon grains studied in this work, which plot on Figure A1 to the right of the unannealed zircon line confirm TEM evidence that radiation damage in these samples has been partially healed. A similar observation was made in a number of zircon samples from a suite of 2.6 Ga (U-Pb age) crystals from Jack Hills studied byNasdala et al. (2001), which are also plotted on Figure A1. The incomplete retention of radiation damage in these samples can be ascribed to either self-annealing processes or recrystallization. Annealing of radiation damage has been reported in several suites of zircon including samples from Sri Lanka, which have calculated dose 0.16 to 0.47 dpa but are not full amorphous by TEM or micro-Raman spectroscopy (Palenik et al., 2003; Nasdala et al., 2004).

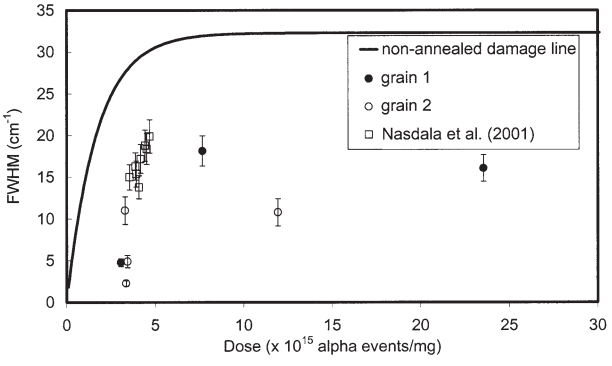

Fig. A1. Micro-Raman spectroscopy data. A plot of FWHM (cm^{-1}) vs. dose ($\times 10^{15}$ α-events/mg). Dose is calculated based on the age of the Jack Hill zircon crystal (−3.3 Ga) and U and Th measured by EMPA. Grain 1 (solid circles) is shown in Figure 1e. Grain 2 (solid is another 3.3 Ga zircon collected from the same locality (01-JH-54). The open square data are from a 2.6 Ga Jack Hill zircon measured by Nasdala et al. (2001). The solid line represents the calibration line determined by Palenik et al. (2003) and Nasdala et al. (2004) for unannealed zircon. FWHM values have an error bar of 10%, while the error on dose calculations is equal to roughly the width of the symbol.